INTERNATIONAL JOURNAL OF AUTOMOTIVE AND MECHANICAL ENGINEERING
ISSN: 2229-8649 e-ISSN: 2180-1606
VOLUME 22, ISSUE 4, 2025, 13086 - 13103
DOI: https://doi.org/10.15282/ijame.22.4.2025.19.0996

RESEARCH ARTICLE

# Experimental and Numerical Investigation of 3D-Printed Spoiler Deflection Under Cantilever Beam Conditions

**Luigi Buffone[1,2]*, Georgios Manganos[2], Kavitha Mol S[3]**

[1]Department of School of Automotive Engineering, Wuhan University of Technology (WUT), Wuhan, Hubei, China
[2]Faculty of Engineering Mechanics, Slovak University of Technology in Bratislava (STU), Bratislava, Slovakia
[3]Department of Mechanical Engineering, Government Polytechnic College, Ezhukone, 691505, Kollam, Kerala, India

**ABSTRACT –** This study presents an experimental and numerical investigation of a high-camber automotive spoiler fabricated using Multi Jet Fusion (MJF) additive manufacturing with two materials: unfilled Nylon PA12 and glass-bead-reinforced PA12 (PA12GB). A total of eight spoiler specimens, representing four aspect ratios for each material, were tested under cantilever beam conditions to evaluate their deflection and strain response under varying concentrated loads. The deformation behavior was captured using strain gauge sensors integrated into a low-cost data acquisition system and validated through Finite Element Analysis (FEA). Results indicate that PA12 exhibits a nonlinear deflection trend at higher loads, while PA12GB maintains a largely linear elastic response. Vertical deflection was found to be the predominant deformation mode, with minimal lateral displacement or rotation. The comparison between experimental and numerical results showed a close correlation, with deviations ranging from 4.8% to 7.2%. This confirms the robustness and reliability of the finite element model. Overall, the study demonstrates that MJF-based additive manufacturing can produce lightweight, structurally efficient and cost-effective spoilers suitable for customized automotive applications.

**ARTICLE HISTORY**
Received : 08th May 2025
Revised : 07th Nov. 2025
Accepted : 18th Nov. 2025
Published : 20th Dec. 2025

**KEYWORDS**
*3D printing*
*Finite element analysis*
*Additive manufacturing*
*Spoiler deflection*
*Structural performance*

## 1. INTRODUCTION

Additive Manufacturing (AM) has become an integral part of modern engineering, with widespread applications in the aerospace, automotive, and biomedical sectors due to its capability to produce complex geometries with high dimensional accuracy and design flexibility [1]. Unlike conventional subtractive manufacturing, AM builds components layer by layer directly from Computer-Aided Design (CAD) models, minimizing tooling requirements and enabling rapid prototyping, lightweight design, and product customization [2, 3]. The choice of AM process, such as Fused Deposition Modeling (FDM), Fused Filament Fabrication (FFF), Powder Bed Fusion (PBF), or Multi Jet Fusion (MJF), depends on the feedstock material, which may be polymers, composites, ceramics, or metals [4].

Recent research has shown notable advancements in the mechanical characterization of additively manufactured (AM) beams and structural components. Building on the foundation laid by early work such as Bandyopadhyay and Heer [5], who emphasised multi-material AM as a route to enhanced mechanical performance, recent studies have significantly expanded the design space and the range of material combinations. For example, a review by Verma et al. [6] systematically examines the state of the art in multi-material AM, covering combinations of polymers, metals, ceramics, and graded compositions, and shows how spatial control of material deposition enables the tailoring of local stiffness, strength, and functionality. Setter and Wudy [7] reviewed that metallic and polymeric AM components can achieve high-performance mechanical parts.

In a more applied context, Lopes et al. [8] demonstrated the industrial feasibility of a multi-functional part made by powder-bed fusion, combining different materials or grades within the same component to meet conflicting design demands (e.g., stiffness vs. impact resistance). Eskandari Sabzi et al. [9] reviewed sustainable polymer AM and noted the importance of optimizing material use in functional components. Furthermore, recent experimental advances strengthen the case for hybrid and multi-material structures in load-bearing applications. Studies on powder-based AM processes have further highlighted the influence of layer orientation, porosity, and material reinforcement on flexural stiffness and failure mechanisms [5–11].

In the automotive sector, AM has been increasingly applied to aerodynamic devices such as spoilers, diffusers, and air ducts, for which lightweight construction and surface precision are critical for performance and energy efficiency [12–14]. Song et al. [12] investigated the free vibration characteristics of composite plates inspired by beetle elytra; Ma et al. [13] conducted numerical analyses on Kevlar/Glass/Epoxy hybrid laminates; and Merzuki et al. [14] experimentally tested fibre-metal composite laminates, pointing out the relevant effects of boundary conditions, stacking sequence, and material reinforcement on vibrational responses. These results, together, highlight the need for integrating experimental and numerical validation when assessing AM components for structural applications.

*CORRESPONDING AUTHOR | L. Buffone | ✉ luigibuffone@yahoo.com

Although additive manufacturing is often credited with reducing material waste, the sustainability advantage depends on the process type, material, and requirements for post-processing. For example, compared to conventional machining, polymer-based techniques such as MJF achieve higher material-use efficiency; however, unsintered powder reuse and thermal degradation may reduce efficiency. In powder-based metal AM, powder recycling and reconditioning can lower overall sustainability improvements due to energy-intensive processing steps. Therefore, mechanical performance, material efficiency, and manufacturing consistency must be considered comprehensively when assessing AM components, especially for critical automotive and other high-performance structural applications. In addition, investigations into the free vibration behavior of advanced composite and hybrid laminates provide complementary insights into dynamic mechanical performance, which is critical for load-bearing structures [15–17].

In the automotive and racing industries, AM has enabled the production of complex, lightweight parts, including brackets, housings, and aerodynamic devices [7, 8]. In light of this perspective, the present study focuses on the design, manufacturing, and mechanical characterization of a high-camber automotive spoiler produced through the Multi Jet Fusion (MJF) process. The MJF process, developed by Hewlett-Packard, utilizes multiple inkjet arrays to selectively fuse polymer powders. It produces parts that exhibit very good dimensional accuracy, surface finish, and reproducibility [2]. Among the various feedstocks supplied so far, Polyamide 12 (PA12) and its glass-bead-reinforced version (PA12GB) have demonstrated superior stiffness, wear resistance, and impact strength, making them suited for mechanically loaded automotive parts [5, 11].

In this study, the printed spoiler was tested experimentally under cantilever beam loading to assess its flexural response. A complementary finite element analysis in ANSYS Mechanical was performed using identical boundary conditions, material parameters, and load configurations to predict deflection. A mesh sensitivity study ensured the reliability of the numerical model. The experimental and simulated results were comparatively analyzed to validate the FEA framework and quantify deviations.

The main aims of this research are:

i) To design and fabricate a high-camber automotive spoiler using PA12 material through MJF additive manufacturing.

ii) To experimentally evaluate the flexural behavior of the printed spoiler under cantilever beam loading.

iii) To develop a validated finite element model to predict structural deflection and compare it with laboratory results.

iv) To analyze the accuracy and consistency between experimental, numerical, and theoretical predictions to identify error margins and validate the AM approach for functional automotive applications.

The proposed research methodology consists of four stages: (i) design and optimization of the CAD geometry of the spoiler; (ii) fabrication of the component by the MJF process using PA12 feedstock; (iii) laboratory-based cantilever loading experiments for measuring deflection; and (iv) model validation and comparative finite element simulations performed in ANSYS. This integrated experimental-numerical approach ensures a systematic evaluation of AM performance for structural automotive components.

## 2. METHODS AND MATERIAL

### 2.1 Design and Fabrication Methodology

The 3D spoiler was fabricated using the Multi-Jet Fusion (MJF) method with the HP Jet Fusion 5200 printer. As shown in Figure 1, the MJF process consists of four steps: (i) preparing a new layer to be built, (ii) depositing fusing and detailing agents onto the polymer powder, (iii) fusing the material using infrared energy, and (iv) cooling and unpacking the finished part [15]. The materials selected for the spoiler were Polyamide 12 (PA12) and Polyamide 12 with Glass Beads (PA12GB).

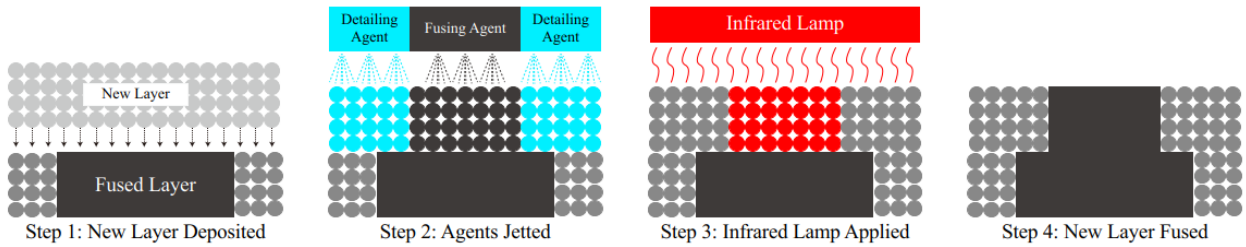


Figure 1. Sketches of the multi-jet fusion (MJF) printing process [15]

PA12 was chosen for its high tensile strength (45–50 MPa), excellent impact resistance, low moisture absorption, and dimensional stability, making it suitable for load-bearing automotive components subjected to cyclic loads and environmental variations. Its semi-crystalline structure further enhances stiffness and fatigue endurance.

PA12GB is a composite variant of PA12 reinforced with approximately 40% glass beads. This reinforcement increases the modulus of elasticity, improves dimensional accuracy, reduces thermal deformation, and maintains adequate toughness, ensuring that the printed component retains its shape and function under aerodynamic and mechanical loads

[18,19]. Together, PA12 and PA12GB provide an ideal comparison between unreinforced and reinforced polymers under identical manufacturing and loading conditions, allowing investigation of the material's influence on deflection behaviour, structural integrity, and the correlation between experimental and numerical results. Both materials exhibit stable mechanical performance across the typical automotive temperature range (−20°C to 80°C). The glass transition temperature (Tg) of PA12 is approximately 45–50°C, above which stiffness and tensile strength gradually decrease. Within the operational range, PA12 maintains sufficient rigidity and impact resistance. The glass bead reinforcement in PA12GB further improves thermal stability, reducing creep and dimensional changes at elevated temperatures [20]. To account for thermal effects, experimental tests were conducted under controlled ambient conditions, while the material properties used in finite element simulations were taken at room temperature (23°C). Future studies could incorporate temperature-dependent material models for more realistic simulations.

The 3D spoiler was printed on an HP Jet Fusion 5200 printer using the Multi-Jet Fusion (MJF) process. The printer produces layers of approximately 0.08 mm thickness at a production rate of 4115 cm³/h [18,19]. The HP MJF technology can produce layers with a thickness of approximately 0.08 mm at a production speed of 4115 cm³/h [18].

### 2.2 Numerical Analysis

The spoiler has a width of 100 mm (chord) and a length of 400 mm (4 times the chord), with a thickness of 9 mm and a maximum camber of 6 mm (9% and 6% of the chord length, respectively). The elastic axis is located 42 mm from the leading edge, where the force is applied to ensure pure bending. The spoiler volume is 0.000247 m³, surface area 0.082958 m², and the moment of inertia along the Y-axis is 3,515.7 kg·mm² (Figure 2). To model the PA12 and PA12GB spoilers, the J2 elastoplastic law is used, with the PA12GB material containing glass beads that increase isotropic hardening. The J2 elastoplastic law is a classical model for isotropic plasticity, where yielding is governed by the second invariant of the deviatoric stress tensor (J2). It defines the transition from elastic to plastic behavior based on a yield criterion, commonly expressed as [20]:

$$f(\sigma) = \sqrt{\frac{3}{2}\mathbf{s}:\mathbf{s}} - \sigma_y = 0 \tag{1}$$

where s is the deviatoric stress tensor and $\sigma_y$ is the yield stress.

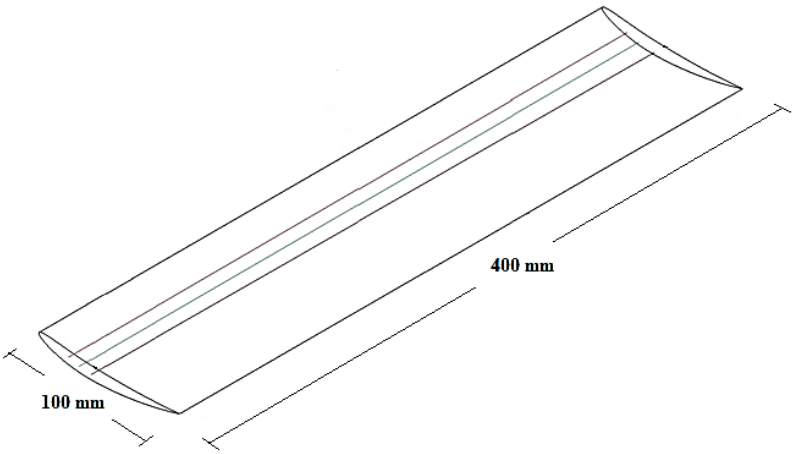


(a)

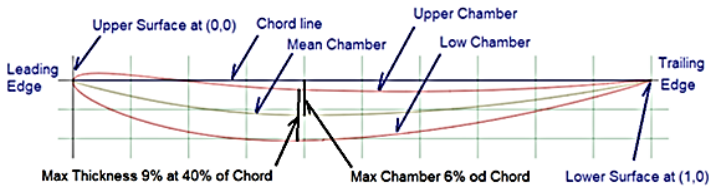


(b)

Figure 2. Spoiler (a) 3D view (b) cross-section

The J2 model is particularly suitable for polymers like PA12 and particulate-reinforced composites like PA12GB, which exhibit isotropic hardening behavior after yielding. For PA12GB, the inclusion of glass beads increases isotropic hardening, which is naturally captured by the J2 formulation [21, 22, 23]. The elastic response was modeled using Hooke's law ($\sigma = E\epsilon$), while plastic deformation was introduced via the J2 yield criterion in finite element simulations. This allowed the analysis to capture both small elastic deflections and large plastic deformations under cantilever loading. For the PA12GB material, which contains discrete glass beads, a 3D transverse isotropic Tsai–Hill failure model was applied to account for stress interactions in the composite. The Tsai–Hill criterion is an extension of the von Mises yield condition to anisotropic composites, expressed as:

$$(\frac{\sigma_1}{X})^2 - \frac{\sigma_1\sigma_2}{X^2} + (\frac{\sigma_2}{Y})^2 + (\frac{\tau_{12}}{S})^2 = 1 \quad (2)$$

where $X, Y$ are the longitudinal and transverse strengths, and $S$ is the in-plane shear strength.

Although the Tsai–Hill model does not capture tension–compression asymmetry or fiber directionality, it provides a conservative estimate of the failure envelope for particulate-reinforced polymers where reinforcement is isotropic (glass spheres rather than fibers) [24,25]. In this study, Tsai–Hill was used to define the onset of plasticity and potential failure in PA12GB, particularly under combined multiaxial stresses induced by cantilever bending. The tensile strength, Young's modulus, and density of PA12 and PA12GB were obtained from official datasheets and the Digimat MF library [26, 27], as given in Table 1. Compared to PA12, PA12GB exhibited an increase of 31.68% in density, 138.03% in modulus of elasticity, and 31.58% in yield strength. These properties were incorporated into the finite element model, which simulated the cantilever beam configuration of the spoiler with one side fixed and a force applied at the free end (Figure 2).

Given the cantilever configuration, the spoiler experiences large deflections near the fixed support. Both geometric and material nonlinearities were considered:

- Elastic domain: Hooke's law ($\sigma = E\epsilon$) for small deformations.

where $\sigma$ is the Normal stress (N/mm$^2$), E is the Modulus of elasticity (MPa), and $\epsilon$ is the Normal strain.

- Plastic domain: J2 elastoplastic law for PA12 and PA12GB.
- Composite failure: Tsai–Hill model for PA12GB.

The deformation at the free end was tracked along both $x$and $y$axes, as well as rotational angles, to accurately capture the spoiler's nonlinear response (Figure 3)

Table 1. Mechanical properties of PA12 and PA12GB of materials

| Mechanical Properties | Value PA12 | Value PA12GB |
|---|---|---|
| Density (gr/cm$^3$) | 1.01 | 1.33 |
| Young's Modulus E (MPa) | 1,128 | 2,685 |
| Poisson's Ratio | 0.39 | 0.37 |
| Tensile Yield Strength (MPa) | 22.8 | 30 |
| Tensile Ultimate Strength (MPa) | 27 | 46 |

The spoiler was modeled as a cantilever beam, fixed at one end and loaded at the free end (Figure 3). Under this configuration, the spoiler experiences small or large deformations depending on the material properties, length, and applied load. The point A at the free end is characterized by two displacement components: $u_x$ along the x-axis and $u_y$ along the y-axis, as well as a rotational angle ($\varphi_0$). In small deformation scenarios, $u_x$ is negligible compared to $u_y$ (Figure 3). However, for nonlinear large deflections, $u_x$ must be considered (Figure 3). The stiffness increase near the fixed support due to large deflections introduces geometric nonlinearity.

The spoiler in question is subjected to large deformations, with point A having two coordinates to consider: $u_x$ is the deformation along the x-axis, and $u_y$ is the deformation along the y-axis, and $\phi_0$ is the rotational angle of the endpoint. Unlike small deformations, where $u_x$ is very small compared to $u_y$ and thus can be neglected in case of a linear problem (refer to Figure 3), but must be considered in case of a nonlinear problem (refer to Figure 3). The increase in stiffness of the spoiler in the cantilever beam configuration is concentrated near the fixed support area, where the large deflection leads to an increase in geometric nonlinearity. In the study of large deflections, based on the Euler-Bernoulli theory, it is necessary to consider higher-order variables, which makes the problem more complex and leads to multiple solutions, each with its respective application limits [28,29]. By applying the correct boundary conditions, solving the higher-order variables through integration, and making the necessary mathematical substitutions, the vertical slope $u_y$can finally be expressed by the following equation [30], [31]:

$$\frac{u_y}{L} = \sqrt{\frac{EI}{2PL^2}} \int_0^{\varphi_0} \frac{sin\,\varphi}{\sqrt{sin\,\varphi_0 - sin\,\varphi}} \quad (3)$$

where L is the length of the spoiler, I is the Area moment of inertia (mm$^4$), and E is Young's Modulus.

Similarly, to the vertical slope, it is possible to calculate the horizontal slope, $u_x$using the equation provided below [30], [31]:

$$\frac{L - u_x}{L} = \frac{EI}{PL^2}\sqrt{2\,sin(\varphi_0)} \quad (4)$$

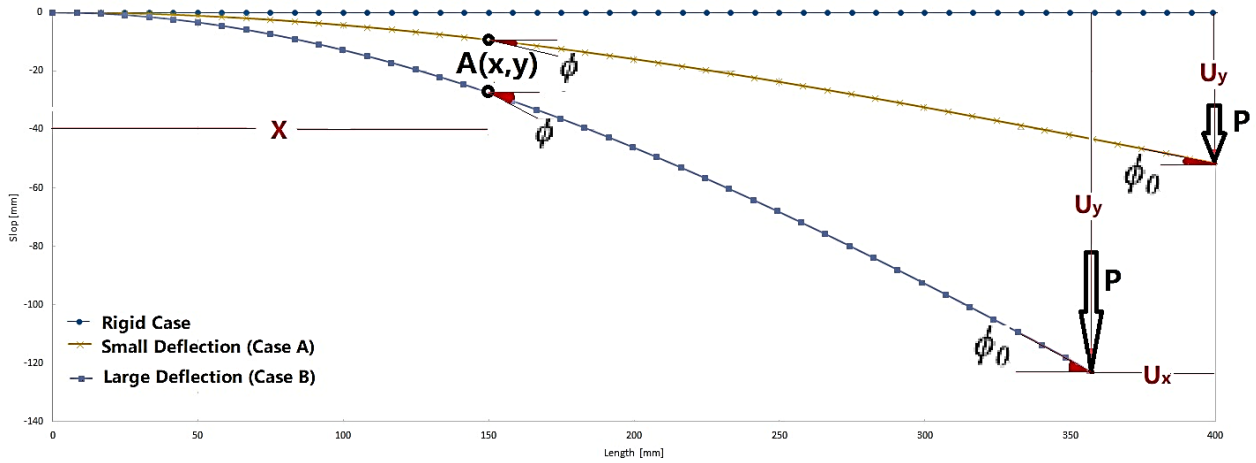


Figure 3. Small and large deformation of cantilever beam

### 2.3 Experimental Setup

To validate the numerical models and accurately characterize the mechanical behavior of the 3D-printed spoiler, laboratory tests were conducted on the Nylon PA12 specimen. These tests were necessary to correlate the finite element simulations with real-world material response under cantilever loading, ensuring that the deflection behavior predicted by the models reflects the actual structural performance of the spoiler. The mechanical properties of the feedstock materials, PA12 and glass-bead-reinforced PA12 (PA12GB), were obtained from the manufacturer's datasheets (EOS GmbH, Germany). To ensure their applicability to the printed components, these properties were further validated through uniaxial tensile testing of printed specimens following ASTM D638 standards. The experimental results confirmed that the datasheet values accurately represent the mechanical behavior of the MJF-printed materials under the tested loading conditions.

The experimental setup, shown in Figure 4, consists of the spoiler sample fixed at one end, with the opposite end free to receive a concentrated load applied using metal discs. This configuration replicates the cantilever boundary conditions used in the simulations, allowing a direct comparison between experimental and numerical results.

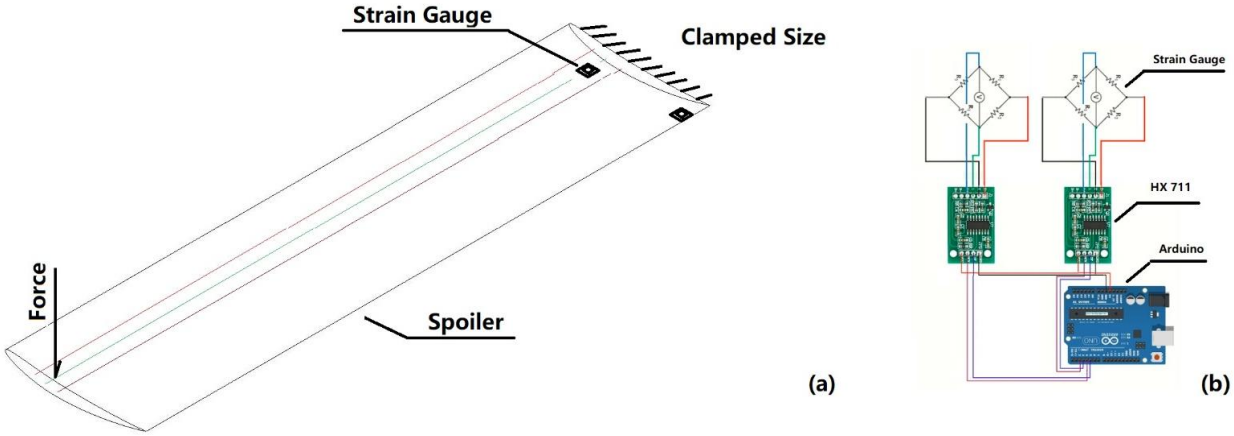


Figure 4. Load test of (a) deflection spoiler (b) electric scheme of LCDAQ

To measure flexural deformations, BF1K-3EB load cells with a total sensing area of 12 × 10 mm² [32,33] were employed. These were connected to a Low-Cost Data Acquisition (LCDAQ) system built around an Arduino UNO microprocessor, operating at 1000 Hz, with custom code developed for data collection. Strain gauge sensors were strategically placed near the fixed support, where deflection is minimal but bending and torsional stresses are highest [34]. The HX711 24-bit amplifier interfaces with the full bridge for amplifying the voltage difference from the strain gauges. The power channels (E+ and E−) supply the sensors, while the voltage channels (A+ and A−) capture the differential output. The amplifier gain can be set to 128 or 64, corresponding to a full-scale differential input voltage of ±20 mV or ±40 mV, respectively (Figure 4) [35]. Data acquired from the Arduino microcontroller were recorded on a laptop using the Arduino IDE software and subsequently exported to a LibreOffice spreadsheet for processing and analysis. This experimental procedure provides a reliable benchmark for validating the numerical models, enabling accurate evaluation of both PA12 and PA12GB spoiler performance under cantilever bending.

### 2.4 Mesh Sensitivity Analysis

To accurately capture the structural response of the spoiler under cantilever loading, ANSYS Mechanical, a Finite Element Analysis (FEA) software, was employed. Specifically, ANSYS Mechanical for Computational Structural Statics (CSS) was used to perform quasi-static simulations, ensuring negligible inertial effects due to low deformation velocities.

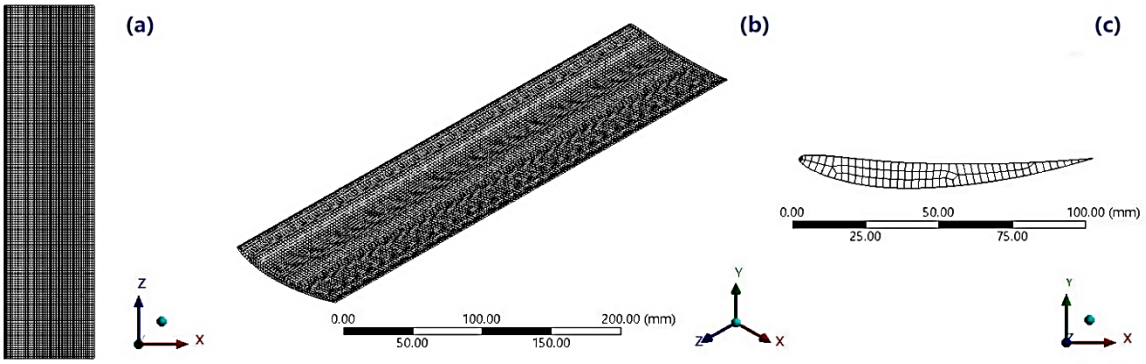


Figure 5. Case study problem mesh (a) Frontal view (b) Isometric view (c) Top view

The spoiler was modelled in a cantilever beam configuration, where one end was fully constrained, and the opposite end was left free. It was subjected to a concentrated vertical load equivalent in magnitude to that applied during the experimental tests. The spoiler geometry was discretised using hexahedral (brick) elements. These elements were selected for their superior accuracy in simulating bending-dominated behaviour compared to tetrahedral meshes. This mesh configuration provided enhanced precision in capturing both bending and torsional deformations (see Figure 5). The size of the mesh cells has a critical impact on the results, making the study of mesh independence essential. This involves finding the cell size that does not significantly influence the variation in bending and twisting in the examined case. Typically, finer meshes yield more accurate results, whereas coarse meshes produce rough approximations. Increasing the number of nodes and cells in the mesh significantly lengthens the simulation time, whereas coarser meshes help reduce computational costs. A mesh independence study was carried out using the PA12 spoiler model to ensure that the simulation results were not significantly affected by mesh density. To select an appropriate fine mesh for the studied spoiler, the mesh was refined iteratively until the results converged.

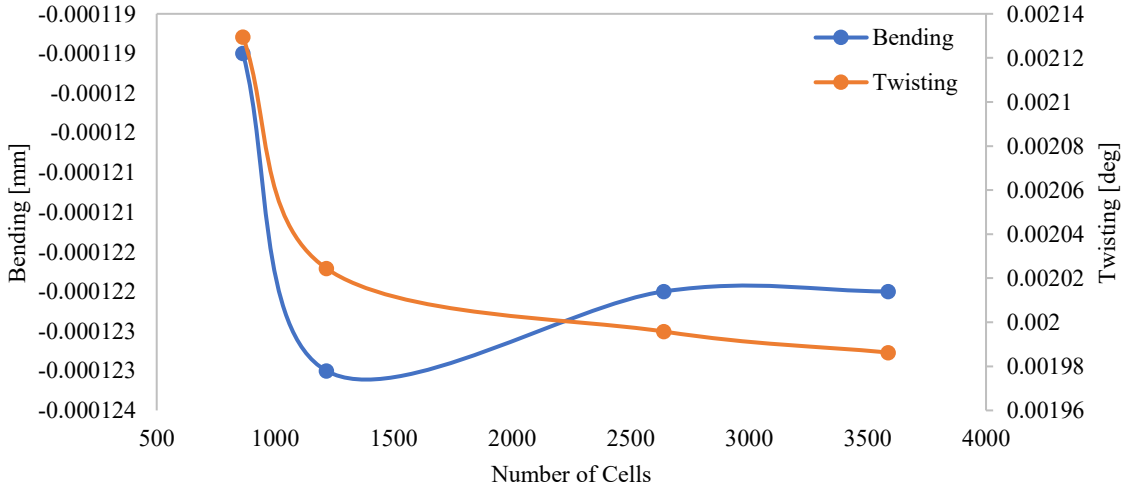


Figure 6. Mesh sensitivity analysis for bending and twisting

The mesh independency study selected four meshes with different numbers of cells: SH1 with 864 cells, SH2 with 1,216 cells, SH3 with 2,640 cells, and SH4 with 3,588 cells. The results under control were spoiler deformations in bending and twisting, with results reported in Figure 6. The deformations were analyzed along the axes corresponding to the maximum bending and torsional responses. Based on the minimal variation between the SH3 and SH4 mesh configurations, the SH3 mesh was selected as the most suitable, providing a balance between computational efficiency and numerical accuracy. The SH3 mesh exhibited an average element quality of 0.9075, with minimum and maximum aspect ratios of 1.002 and 384.6, respectively. The average skewness was 0.15483, while the minimum and maximum orthogonal qualities were $6.8073 \times 10^{-4}$ and 0.99995, respectively (see Table 2).

Table 2. FEA mesh independency

| Mesh Name | Cells | Bending [mm] | Twisting [°] | Bend Var. | Twist Var. |
|---|---|---|---|---|---|
| SH1 | 864 | -0.000119 | 0.002129493 | 0% | 0% |
| SH2 | 1,216 | -0.000123 | 0.002024451 | -1.19% | -1.08% |
| SH3 | 2,640 | -0.000122 | 0.001995803 | -1.05% | -1.009% |
| SH4 | 3,588 | -0.000122 | 0.001986254 | -0.025% | -0.016% |

## 3. RESULTS AND DISCUSSION

The mechanical response of the high-camber automotive spoiler was analyzed using a cantilever beam model, where one end is fixed, and the other has six degrees of freedom (three translational, three rotational). Loads were applied incrementally from -4 N to -40 N with a step of 4 N using 1000 sub-steps to ensure solver convergence. Maximum vertical displacements of -70.83 mm (PA12) and -144.82 mm (PA12GB) were observed. Initial responses were linear, transitioning to nonlinear behavior at higher loads, addressed via the Newton-Raphson method. Nonlinear behavior is associated with large deformations, rotations, and stress stiffening/softening. To analyze trends, the spoiler length was divided into four 100 mm sections, representing different aspect ratios (AR1–AR4): AR1: 100 mm, AR2: 200 mm, AR3: 300 mm, and AR4: 400 mm.

### 3.1 Spoiler with AR1

In this section, the endpoint displacements at $L = 100$ mm from the fixed support were analyzed for both $PA12_{AR1}$ and $PA12GB_{AR1}$ materials using experimental measurements and FEA predictions. The first spoiler segment, located near the fixed end with a length of 100 mm, is shown in Figure 7. To distinguish between linear and nonlinear deformation, a strain-based threshold relative to the material yield point was established. For $PA12_{AR1}$, linear behavior was assumed when the maximum tensile strain remained below 0.5%, corresponding to the elastic regime of the polymer as confirmed by the stress–strain data; beyond this limit, plasticity developed, indicating nonlinear behavior. Similarly to $PA12_{AR1}$, a linear behavior was also defined for $PA12GB_{AR1}$ for deformations lower than 0.4%, consistent with the stiffer response of the glass fiber reinforced composite. Within the elastic regime, both $u_y/L$, $u_x/L$, and the rotation angle exhibited proportional increases with the applied load, consistent with linear elasticity (Figure 7). However, once the applied load exceeded the elastic threshold, the stress–strain response departed from linearity, requiring nonlinear analysis methods (Figure 7).

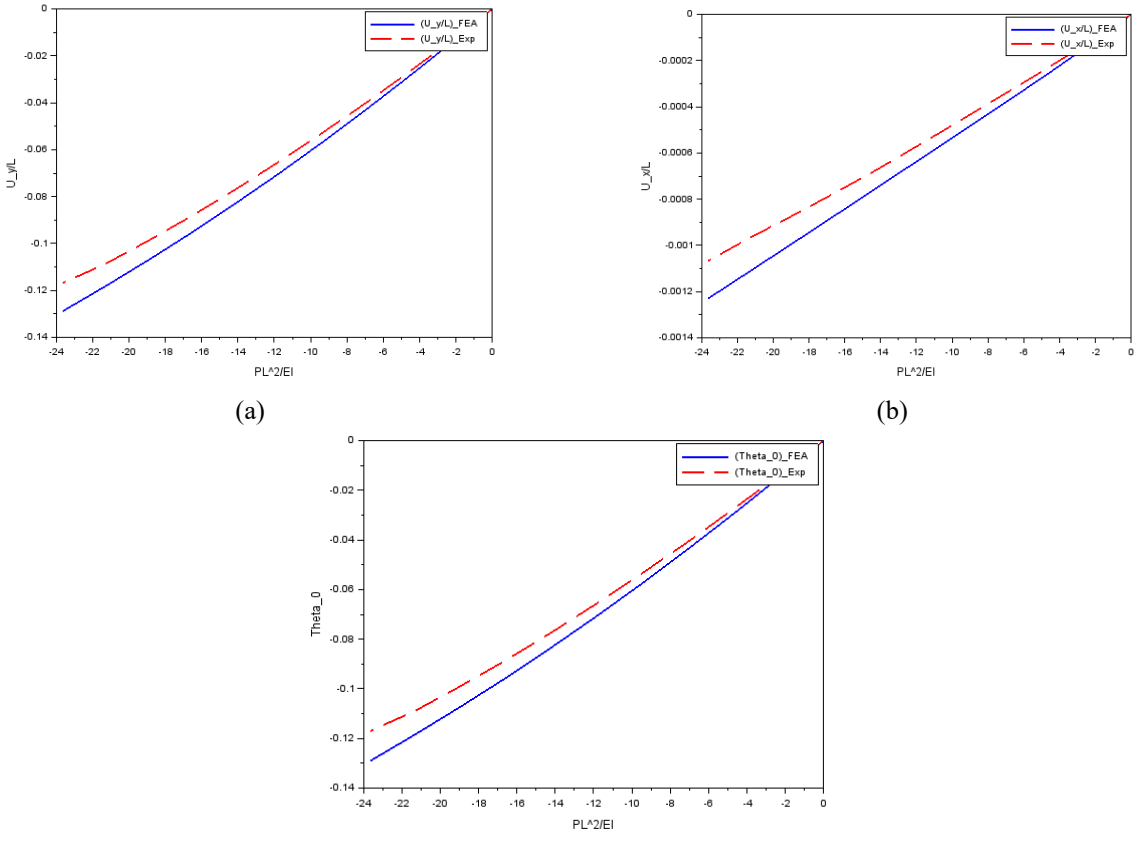


Figure 7. Comparison of $PA12_{AR1}$ (a) $u_y/L$ (b) $u_x/L$ and (c) $\phi_0$ of endpoint under various loads

The comparison between experimental and FEA results demonstrated good agreement in both the linear and nonlinear regimes, though deviations increased under higher loads. For $u_y/L$, the minimum and maximum errors were 6.11% and 9.31%, respectively; for $u_x/L$, the error ranged from –10.04% to –13.21%; and for the rotation angle, discrepancies varied between –6.12% and –9.31% (Table 3). The divergence between experimental and FEA outcomes for the $PA12_{AR1}$ spoiler increased with load, particularly in the nonlinear deformation range. These deviations can be attributed to material property variations due to additive manufacturing, including local differences in density, crystallinity, and modulus; geometric deviations from print tolerances; minor compliance at the experimental fixture; and inherent FEA modeling limitations such as isotropy assumptions and discretization approximations. Despite these factors, the overall deviations ranging from 6% to 13% are within acceptable limits for polymer-based additive-manufactured components.

Table 3. Comparison of slope endpoint for $PA12_{AR1}$ material

| $PL^2/EI$ | Vertical Deflection $PA12_{AR1}$ | | | Horizontal Deflection $PA12_{AR1}$ | | | Rotation $PA12_{AR1}$ | | |
|---|---|---|---|---|---|---|---|---|---|
| | $(u_y/L)$ FEA | $(u_y/L)$ Exp | Error | $(u_x/L)$ FEA | $(u_x/L)$ Exp | Error | $\phi_0$ FEA | $\phi_0$ Exp | Error |
| 0 | 0 | 0 | 0% | 0 | 0 | 0% | 0 | 0 | 0% |
| -2.3649 | -0.0150 | -0.0141 | 6.11% | -0.0001 | -0.0001 | -10.04% | -0.0151 | -0.0141 | -6.12% |
| -4.7298 | -0.0296 | -0.0277 | 6.60% | -0.0002 | -0.0002 | -10.07% | -0.0297 | -0.0277 | -6.61% |
| -7.0947 | -0.0437 | -0.0408 | 6.71% | -0.0003 | -0.0003 | -10.14% | -0.0438 | -0.0408 | -6.72% |
| -9.4596 | -0.0574 | -0.0533 | 7.11% | -0.0005 | -0.0004 | -10.18% | -0.0575 | -0.0534 | -7.12% |
| -11.824 | -0.0706 | -0.0655 | 7.21% | -0.0006 | -0.0005 | -10.28% | -0.0706 | -0.0655 | -7.20% |
| -14.189 | -0.0832 | -0.0772 | 7.19% | -0.0007 | -0.0006 | -10.40% | -0.0833 | -0.0772 | -7.20% |
| -16.554 | -0.0954 | -0.0883 | 7.41% | -0.0008 | -0.0007 | -11.21% | -0.0955 | -0.0884 | -7.42% |
| -18.919 | -0.1070 | -0.0987 | 7.74% | -0.0009 | -0.0008 | -12.09% | -0.1071 | -0.0988 | -7.75% |
| -21.284 | -0.1181 | -0.1086 | 8.04% | -0.0011 | -0.0009 | -13.02% | -0.1183 | -0.1088 | -8.04% |
| -23.648 | -0.1288 | -0.1168 | 9.31% | -0.0012 | -0.0010 | -13.21% | -0.1290 | -0.1169 | -9.32% |

The results confirm that the FEA model effectively captures both the elastic and plastic responses of the PA12AR1 spoiler under cantilever loading while accounting for the influence of manufacturing and boundary conditions. The largest deviations, around 13%, occurred under high-load conditions where geometric and material nonlinearities are most significant, validating the accuracy and reliability of the numerical model.

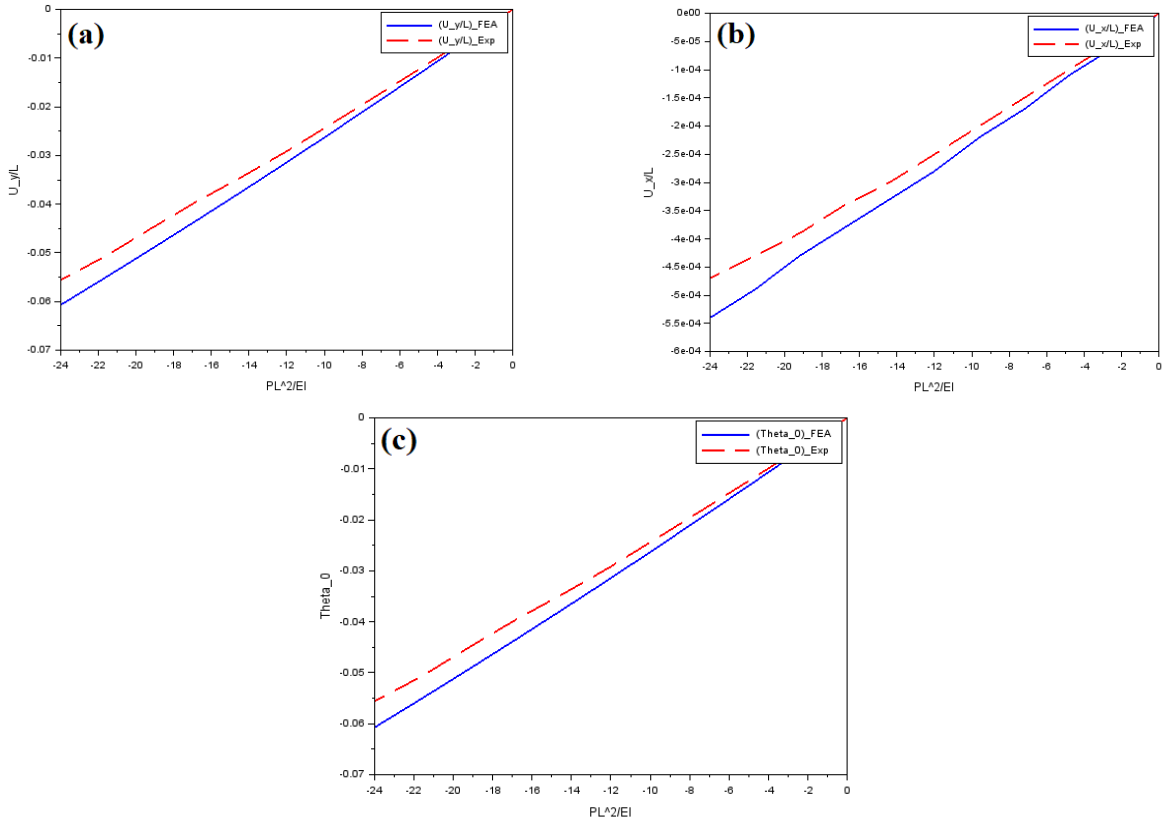


Figure 8. Comparison of $PA12GB_{AR1}$ (a) $u_y/L$ (b) $u_x/L$ and (c) $\phi_0$ of endpoint under various loads

Unlike the PA12 spoiler, the spoiler made of $PA12GB_{AR1}$ material exhibited linear trends for $u_y/L$, $u_x/L$, and the endpoint rotation at $L = 100$ mm across the entire range of applied loads. This linear relationship indicates that both the experimental and FEA results increased proportionally with the applied load, confirming that linear and nonlinear analysis methods yield consistent outcomes for this material (Figure 8). In the case of $PA12GB_{AR1}$, the comparison between experimental and FEA predictions revealed a slight but systematic divergence that increased with load, similar to the behavior observed for $PA12_{AR1}$. Specifically, for $u_y/L$, the minimum and maximum errors were 7.13% and 8.44%, respectively; for $u_x/L$, the deviations ranged from –10.11% to –12.11%; and for the rotation angle $\theta$, the discrepancies varied between –7.13% and –8.44% (Table 4).

Overall, when comparing both materials, the $PA12_{AR1}$ spoiler showed a clear transition from linear to nonlinear behavior as the applied load increased beyond the elastic threshold, while the $PA12GB_{AR1}$ spoiler maintained linearity throughout due to its higher stiffness and reduced deformability. The observed deviations between experimental and FEA results, ranging from 6% to 13% for $PA12_{AR1}$ and 7% to 12% for $PA12GB_{AR1}$ are within acceptable limits for polymer-based additive-manufactured components. These findings confirm that the numerical models accurately capture the deformation responses of both materials under cantilever loading, with the $PA12GB_{AR1}$ exhibiting superior dimensional stability and reduced sensitivity to nonlinear effects compared to $PA12_{AR1}$.

Table 4. Comparison of slope endpoint for $PA12GB_{AR1}$ material

| $PL^2/EI$ | Vertical Defl. $PA12GB_{AR1}$ | | | Horizontal Defl. $PA12GB_{AR1}$ | | | Rotation $PA12GB_{AR1}$ | | |
|---|---|---|---|---|---|---|---|---|---|
| | $(u_y/L)_{FEA}$ | $(u_y/L)_{Exp}$ | Error | $(u_x/L)_{FEA}$ | $(u_x/L)_{Exp}$ | Error | $\phi_{0\ FEA}$ | $\phi_{0\ Exp}$ | Error |
| 0 | 0 | 0 | 0% | 0 | 0 | 0% | 0 | 0 | 0% |
| -2.3986 | -0.00642 | -0.00595 | 7.13% | -0.00006 | -0.00005 | -10.11% | -0.00642 | -0.0059 | -7.13% |
| -4.7971 | -0.01276 | -0.01184 | 7.15% | -0.00011 | -0.00010 | -10.11% | -0.01276 | -0.0118 | -7.15% |
| -7.1957 | -0.01903 | -0.01766 | 7.18% | -0.00017 | -0.00015 | -10.13% | -0.01904 | -0.0176 | -7.18% |
| -9.5942 | -0.02525 | -0.02343 | 7.21% | -0.00022 | -0.00020 | -10.21% | -0.02526 | -0.0234 | -7.21% |
| -11.993 | -0.03141 | -0.02914 | 7.24% | -0.00028 | -0.00025 | -10.22% | -0.03142 | -0.0291 | -7.24% |
| -14.391 | -0.03744 | -0.03443 | 8.03% | -0.00033 | -0.00030 | -10.12% | -0.03745 | -0.0344 | -8.03% |
| -16.789 | -0.04338 | -0.03950 | 8.94% | -0.00038 | -0.00034 | -10.19% | -0.04340 | -0.0395 | -8.94% |
| -19.188 | -0.04929 | -0.04498 | 8.64% | -0.00043 | -0.00039 | -10.92% | -0.04926 | -0.0450 | -8.64% |
| -21.587 | -0.05501 | -0.05065 | 7.92% | -0.00049 | -0.00043 | -11.91% | -0.05504 | -0.0506 | -7.92% |
| -23.985 | -0.0607 | -0.05556 | 8.44% | -0.00054 | -0.00047 | -12.11% | -0.06072 | -0.0556 | -8.44% |

### 3.2 Spoiler with AR2

This section presents the results and discussion of both experimental and FEA analyses for the vertical deflection, horizontal deflection, and rotation of the spoiler's endpoint located 200 mm from the fixed support. The variation in the radius of curvature for vertical deformation $u_y/L$ was evaluated across the full range of applied loads. The results show a continuous change in curvature, with $u_y/L$ reaching a minimum of –0.2305 for a $PL^2/EI$ value of –94.5955. In contrast, the horizontal deflection $u_x/L$ exhibits a nearly constant radius of curvature, with a maximum deflection of –0.00247 under the same load condition. The endpoint rotation ($\theta$) follows a similar trend to $u_y/L$, showing a variable curvature response throughout the analyzed load range. In this region, both linear and nonlinear theories yield closely matching results, as illustrated in Figure 9.

The comparison between experimental and numerical data at $L = 200$ mm reveals small yet consistent deviations, similar to those observed at $L = 100$ mm. Specifically, the percentage error in vertical deflection $u_y/L$ ranges from a minimum of 6.11% at $PL^2/EI = -2.3649$ to a maximum of 9.31% at $PL^2/EI = -23.468$. For horizontal deflection $u_x/L$, the error varies between –10.04% and –13.21% across the same load range, while for the rotation angle ($\theta$), discrepancies lie between –6.12% and –9.32% (see Table 5). These differences remain within acceptable bounds, confirming the robustness of the numerical model in capturing both the elastic and plastic responses of the spoiler under cantilever loading.

In the case of the $PA12GB_{AR2}$ material, the behavior is distinct. The radius of curvature for both vertical $u_y/L$ and horizontal $u_x/L$ deflections remain constant throughout the applied load range (Figure 10), and the endpoint rotation also displays a constant radius of curvature between $PL^2/EI = 0$ and –95.94. This consistent curvature indicates a linear deformation response with load, allowing both small and large deformation solvers to be used effectively for this material. However, while the FEA results predict a constant curvature across the load range, the experimental results exhibit a mixed behaviour showing a constant radius of curvature in the initial section and a variable one in the later stages, indicating the onset of mild nonlinearity in the experimental response.

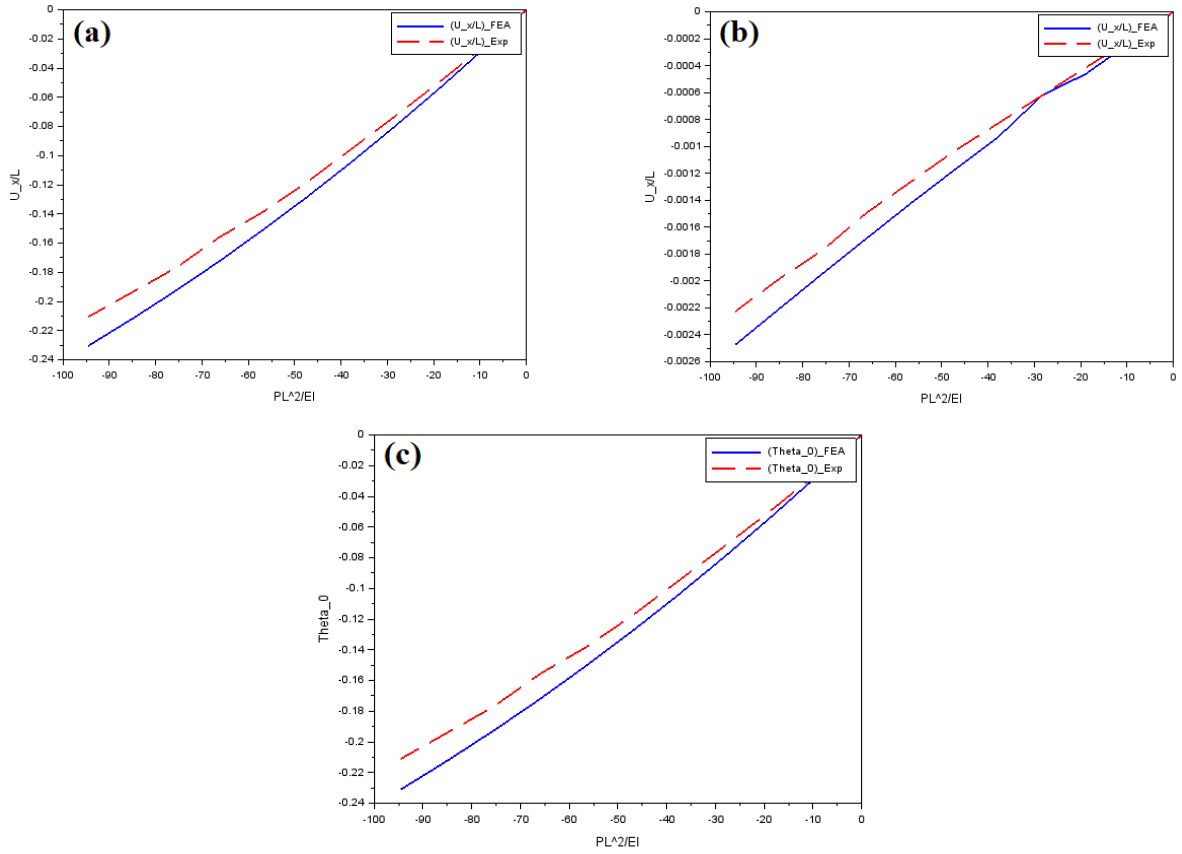


Figure 9. Comparison of $PA12_{AR2}$ (a) $u_y/L$ (b) $u_x/L$ and (c) $\phi_0$ of endpoint under various loads

Table 5. Comparison of slope endpoint for $PA12_{AR2}$ material

| $PL^2/EI$ | Vertical Deflection $PA12_{AR2}$ | | | Horizontal Deflection $PA12_{AR2}$ | | | Rotation $PA12_{AR2}$ | | |
|---|---|---|---|---|---|---|---|---|---|
| | $(u_y/L)$ FEA | $(u_y/L)$ Exp | Error | $(u_x/L)$ FEA | $(u_x/L)$ Exp | Error | $\phi_0$ FEA | $\phi_0$ Exp | Error |
| 0 | 0 | 0 | 0% | 0 | 0 | 0% | 0 | 0 | 0% |
| -2.3649 | -0.0150 | -0.0141 | 6.11% | -0.0001 | -0.0001 | -10.04% | -0.0151 | -0.0141 | -6.12% |
| -4.7298 | -0.0296 | -0.0277 | 6.60% | -0.0002 | -0.0002 | -10.07% | -0.0297 | -0.0277 | -6.61% |
| -7.0947 | -0.0437 | -0.0408 | 6.71% | -0.0003 | -0.0003 | -10.14% | -0.0438 | -0.0408 | -6.72% |
| -9.4596 | -0.0574 | -0.0533 | 7.11% | -0.0005 | -0.0004 | -10.18% | -0.0575 | -0.0534 | -7.12% |
| -11.824 | -0.0706 | -0.0655 | 7.21% | -0.0006 | -0.0005 | -10.28% | -0.0706 | -0.0655 | -7.20% |
| -14.189 | -0.0832 | -0.0772 | 7.19% | -0.0007 | -0.0006 | -10.40% | -0.0833 | -0.0772 | -7.20% |
| -16.554 | -0.0954 | -0.0883 | 7.41% | -0.0008 | -0.0007 | -11.21% | -0.0955 | -0.0884 | -7.42% |
| -18.919 | -0.1070 | -0.0987 | 7.74% | -0.0009 | -0.0008 | -12.09% | -0.1071 | -0.0988 | -7.75% |
| -21.284 | -0.1181 | -0.1086 | 8.04% | -0.0011 | -0.0009 | -13.02% | -0.1183 | -0.1088 | -8.04% |
| -23.648 | -0.1288 | -0.1168 | 9.31% | -0.0012 | -0.0010 | -13.21% | -0.1290 | -0.1169 | -9.32% |

This discrepancy is most evident in the vertical deflection $u_y/L$ and rotation ($\theta$) of the endpoint, whereas the horizontal deflection $u_x/L$ shows a relatively smaller variation. The experimental $u_x/L$ data demonstrate greater variability compared to the corresponding vertical and rotational components. As summarized in Table 6, when $PL^2/EI$ exceeds –67.159, the divergence between FEA and experimental results increases rapidly from 9.83% to 12.76% for vertical deflection and from –9.81% to –12.72% for rotation, while the horizontal deflection maintains a more consistent trend with modest deviations across the load range up to $PL^2/EI = -18.919$. Overall, these results indicate that the FEA model effectively predicts the deformation behavior of both $PA12_{AR1}$ and $PA12GB_{AR2}$ spoilers under cantilever loading, with minor discrepancies arising mainly from experimental nonlinearities, boundary conditions, and manufacturing variations.

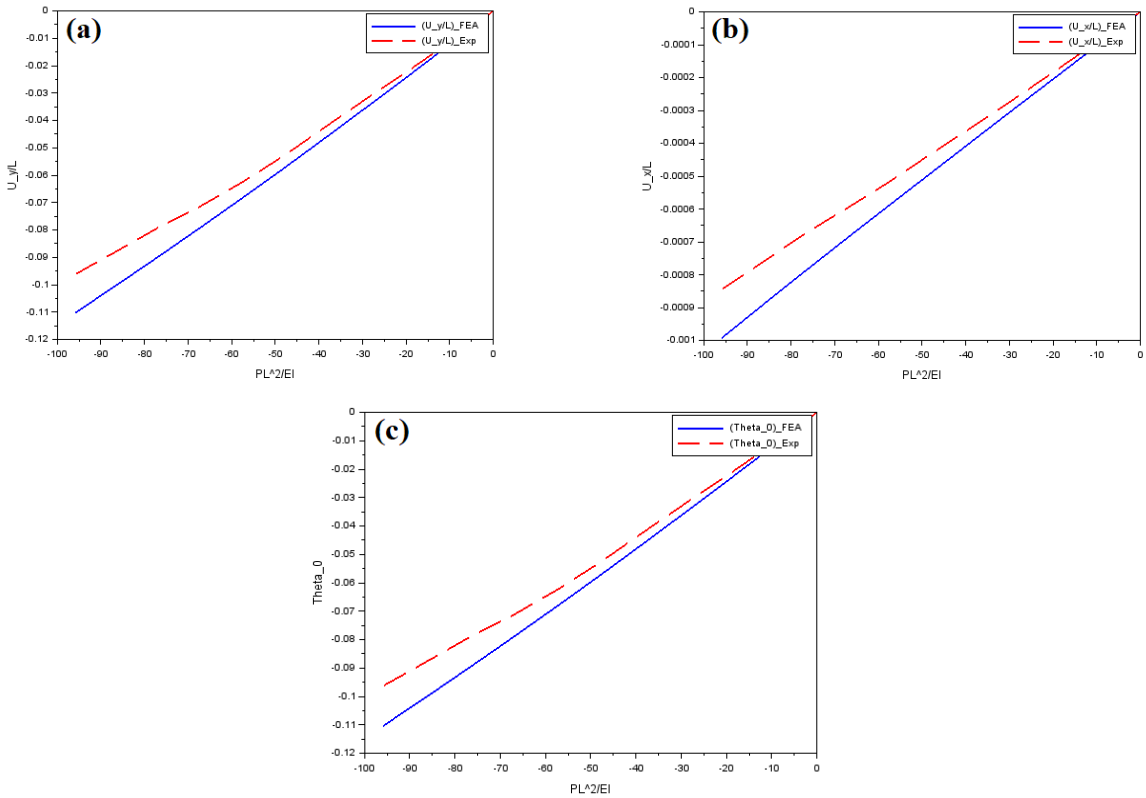


Figure 10. Comparison of PA12GB$_{AR2}$ (a) $u_y/L$ (b) $u_x/L$ and (c) $\phi_0$ of endpoint under various loads

Table 6. Comparison of slope endpoint for PA12GB$_{AR2}$ material

| PL$^2$/EI | Vertical Deflection PA12$_{AR2}$ | | | Horizontal Deflection PA12$_{AR2}$ | | | Rotation PA12$_{AR2}$ | | |
|---|---|---|---|---|---|---|---|---|---|
| | $(u_y/L)$ FEA | $(u_y/L)$ Exp | Error | $(u_x/L)$ FEA | $(u_x/L)$ Exp | Error | $\phi_0$ FEA | $\phi_0$ Exp | Error |
| 0 | 0 | 0 | 0% | 0 | 0 | 0% | 0 | 0 | 0% |
| -9.5942 | -0.01175 | -0.01090 | 7.24% | -00000.9 | -0.00008 | -10.22% | -0.01175 | -0.0109 | -7.24% |
| -19.188 | -0.02336 | -0.02149 | 8.03% | -0.00019 | -0.00018 | -10.12% | -0.02337 | -0.0215 | -8.03% |
| -28.783 | -0.03482 | -0.03171 | 8.94% | -0.00029 | -0.00026 | -10.19% | -0.03483 | -0.0317 | -8.94% |
| -38.376 | -0.04617 | -0.04218 | 8.64% | -0.00039 | -0.00034 | -10.92% | -0.04619 | -0.0422 | -8.64% |
| -47.971 | -0.05739 | -0.05285 | 7.92% | -0.00049 | -0.00043 | -11.91% | -0.05742 | -0.0528 | -7.92% |
| -57.565 | -0.06834 | -0.06257 | 8.44% | -0.00059 | -0.00052 | -12.11% | -0.06838 | -0.0626 | -8.44% |
| -67.159 | -0.07910 | -0.07131 | 9.83% | -0.00068 | -0.00059 | -13.21% | -0.07916 | -0.0714 | -9.81% |
| -76.753 | -0.08969 | -0.07907 | 11.84% | -0.00079 | -0.00067 | -14.51% | -0.08976 | -0.0791 | -11.84% |
| -86.347 | -0.10010 | -0.08772 | 12.36% | -0.00089 | -0.00076 | -14.62% | -0.10019 | -0.0878 | -12.36% |
| -95.942 | -0.11032 | -0.09626 | 12.76% | -0.00099 | -0.00084 | -14.96% | -0.11043 | -0.0963 | -12.72% |

### 3.3 Spoiler with AR3

In this section, the endpoint displacements at L = 300 mm from the fixed support, under various loads, are analyzed for both PA12$_{AR3}$ and PA12GB$_{AR3}$ materials, considering both experimental and FEA results. From the left side of Figure 10, it is possible to observe the nonlinearity of $u_y/L$, which means that this point has a variable radius of curvature and therefore does not increase linearly with increasing load. The rotation of the endpoint also has a nonlinear trend, similar to the vertical deflection point, and is therefore subject to the same law of variable radius of curvature. The horizontal deflection point $u_x/L$ has a nonlinear increasing trend, but with opposite concavity to that of $u_x/L$. The force applied at the end of the spoiler subjected to bending is decomposed into two parts: an axial force (which is tangent to the radius of curvature) and a radial force (which develops along the radius of curvature), see Figure 11.

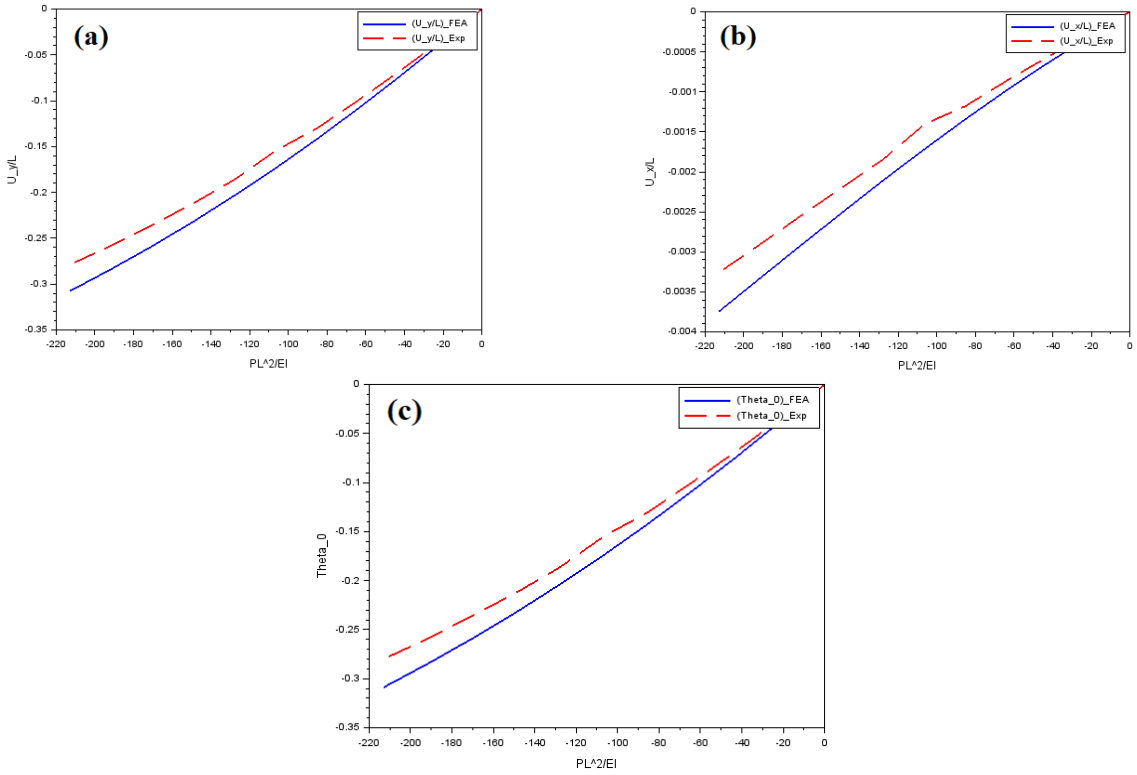


Figure 11. Comparison of $PA12_{AR3}$ (a) $u_y/L$ (b) $u_x/L$ and (c) $\phi_0$ of endpoint under various loads

Regarding the difference between the experimental and FEA results, it is divergently increasing right from the initial values and continues to grow. Specifically, the divergence in both $u_y/L$, $u_x/L$, and ($\phi_0$) is smaller for values of $PL^2/EI$ below -85.1359, while for values of $PL^2/EI$ above -85.1359, the gap increases. The highest percentage difference between the experimental and FEA results occurs when $PL^2/EI$ is equal to -106.42. Here, the difference in $u_y/L$ is 10.98%, while the difference in $u_x/L$ is -18.93%, and the difference in $\phi_0$ is -10.9% (reference to Table 7).

Table 7. Comparison of slope endpoint for $PA12_{AR3}$ material

| $PL^2/EI$ | Vertical Deflection $PA12_{AR3}$ | | | Horizontal Deflection $PA12_{AR3}$ | | | Rotation $PA12_{AR3}$ | | |
|---|---|---|---|---|---|---|---|---|---|
| | $(u_y/L)$ FEA | $(u_y/L)$ Exp | Error | $(u_x/L)$ FEA | $(u_x/L)$ Exp | Error | $\phi_0$ FEA | $\phi_0$ Exp | Error |
| 0 | 0 | 0 | 0% | 0 | 0 | 0% | 0 | 0 | 0% |
| -21.284 | -0.03749 | -0.03452 | 7.924% | -0.00031 | -0.00027 | -11.91% | -0.03749 | -0.0345 | -7.88% |
| -42.568 | -0.07367 | -0.06776 | 8.024% | -0.00064 | -0.00056 | -12.07% | -0.07372 | -0.0678 | -8.02% |
| -63.852 | -0.10833 | -0.09943 | 8.214% | -0.00098 | -0.00086 | -12.15% | -0.10843 | -0.0995 | -8.21% |
| -85.136 | -0.14162 | -0.12987 | 8.300% | -0.00134 | -0.00117 | -12.21% | -0.14182 | -0.1300 | -8.30% |
| -106.42 | -0.17328 | -0.15425 | 10.98% | -0.00172 | -0.00140 | -18.23% | -0.17358 | -0.1545 | -10.9% |
| -127.70 | -0.20318 | -0.18584 | 8.532% | -0.00210 | -0.00184 | -12.43% | -0.20361 | -0.1862 | -8.53% |
| -148.98 | -0.23174 | -0.21178 | 8.612% | -0.00251 | -0.00219 | -12.51% | -0.23233 | -0.2123 | -8.61% |
| -170.27 | -0.25848 | -0.23536 | 8.942% | -0.00291 | -0.00254 | -12.64% | -0.25923 | -0.2360 | -8.94% |
| -191.55 | -0.28373 | -0.25814 | 9.016% | -0.00333 | -0.00291 | -12.70% | -0.28467 | -0.2590 | -9.02% |
| -212.84 | -0.30757 | -0.27877 | 9.361% | -0.00374 | -0.00326 | -13.02% | -0.30872 | -0.2798 | -9.36% |

In the case of the $PA12GB_{AR3}$ spoiler, the point 300 mm from the fixed support has linear vertical and horizontal deflections. This indicates that the radius of curvature remains constant throughout the range of loads analyzed. The angle of rotation, similar to the vertical and horizontal deflections, also has a constant radius of curvature, but with different values compared to the previous ones (reference to Figure 12).

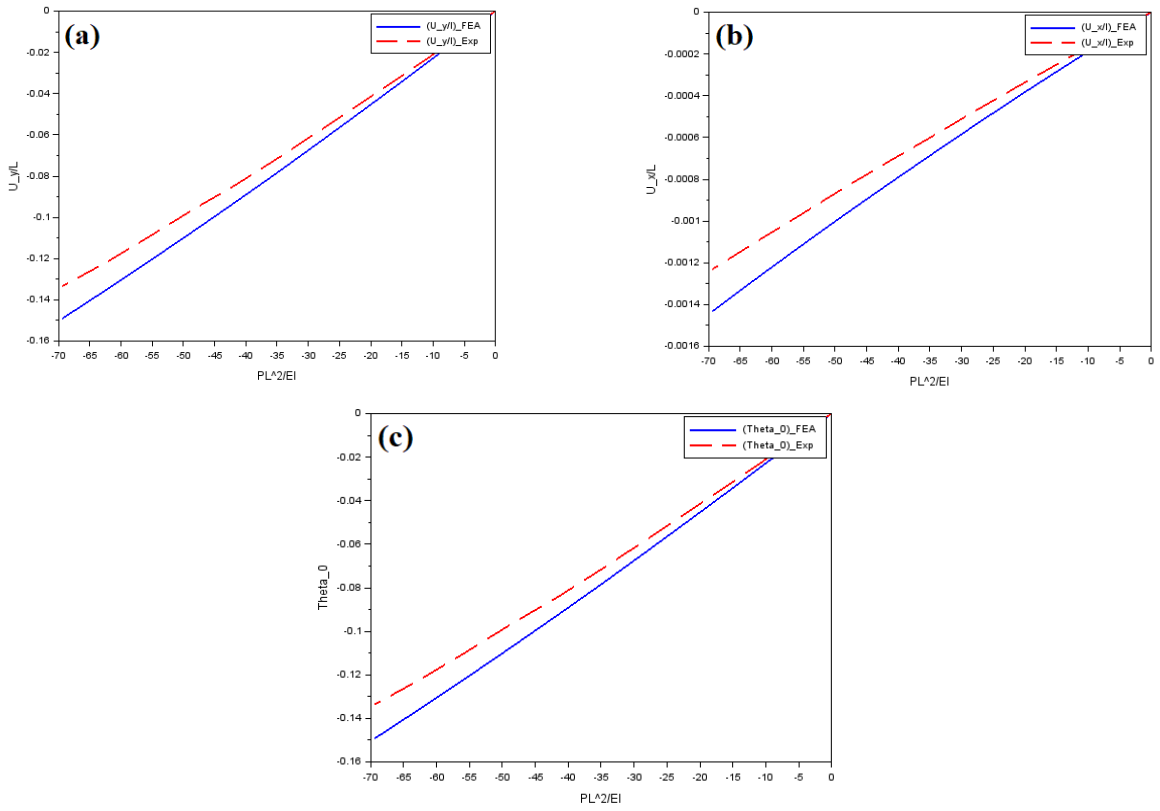


Figure 12. Comparison of $PA12GB_{AR3}$ (a) $u_y/L$ (b) $u_x/L$ and (c) $\phi_0$ of endpoint under various loads

The experimental results are in line with the FEA results but show a slight divergence that increases as the load increases. In detail, $u_y/L$ and $u_x/L$ reach a maximum difference of 12.74% and -14.96% respectively, while the angle of rotation ( $\phi_0$ ) reaches a maximum difference of -12.7% (reference to Table 8).

Table 8. Comparison of slope endpoint for $PA12GB_{AR3}$ material

| $PL^2/EI$ | Vertical Defl. $PA12GB_{AR3}$ | | | Horizontal Defl. $PA12GB_{AR3}$ | | | Rotation $PA12GB_{AR3}$ | | |
|---|---|---|---|---|---|---|---|---|---|
| | $(u_y/L)$ FEA | $(u_y/L)$ Exp | Error | $(u_x/L)$ FEA | $(u_x/L)$ Exp | Error | $\phi_0$ FEA | $\phi_0$ Exp | Error |
| 0 | 0 | 0 | 0% | 0 | 0 | 0% | 0 | 0 | 0% |
| -9.5942 | -0.01175 | -0.01090 | 7.241% | -0.00009 | -0.00008 | -10.22% | -0.01176 | -0.0109 | -7.24% |
| -19.188 | -0.02336 | -0.02149 | 8.034% | -0.00019 | -0.00017 | -10.12% | -0.02337 | -0.0215 | -8.03% |
| -28.782 | -0.03482 | -0.03171 | 8.940% | -0.00029 | -0.00026 | -10.19% | -0.03483 | -0.0317 | -8.94% |
| -38.376 | -0.04617 | -0.04218 | 8.641% | -0.00039 | -0.00034 | -10.92% | -0.04619 | -0.0422 | -8.64% |
| -47.971 | -0.05739 | -0.05284 | 7.924% | -0.00049 | -0.00043 | -11.91% | -0.05742 | -0.0528 | -7.92% |
| -57.565 | -0.06834 | -0.06257 | 8.443% | -0.00059 | -0.00052 | -12.11% | -0.06838 | -0.0626 | -8.44% |
| -67.159 | -0.07910 | -0.07132 | 9.844% | -0.00068 | -0.00059 | -13.21% | -0.07916 | -0.0714 | -9.84% |
| -76.753 | -0.08969 | -0.07907 | 11.84% | -0.00078 | -0.00067 | -14.51% | -0.08976 | -0.0791 | -11.8% |
| -86.348 | -0.10010 | -0.08773 | 12.36% | -0.00089 | -0.00076 | -14.62% | -0.10019 | -0.0878 | -12.3% |
| -95.940 | -0.11032 | -0.09626 | 12.74% | -0.00099 | -0.00084 | -14.96% | -0.11043 | -0.0964 | -12.7% |

### 3.4 Spoiler with AR4

The spoiler section analyzed in this section has an aspect ratio (AR) of 4, which means a length of 400 mm. Here, the load applied to the spoiler varies from 0 to -212.8399 $PL^2/EI$, and it was possible to observe the nonlinear responses of vertical deflection $u_y/L$, horizontal deflection $u_x/L$, and rotation angle ( $\phi_0$ ) for the $PA12_{AR4}$ material (refer to Figure 13, left and right). The results have a variable radius of curvature, which means the area is subject to nonlinear deformation, and only solution methods that take into account large deformations of the spoiler can be applied.

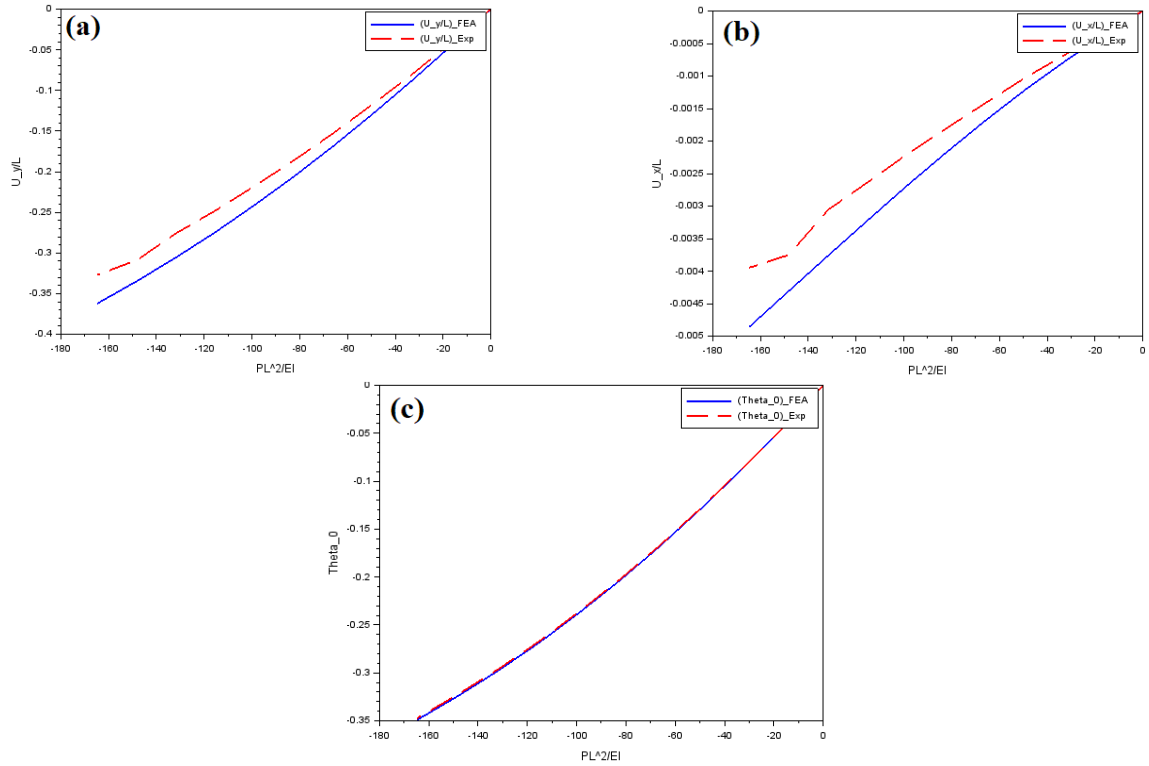


Figure 13. Comparison of $PA12_{AR4}$ (a) $u_y/L$ (b) $u_x/L$ and (c) $\phi_0$ of endpoint under various loads

The divergence between the experimental and FEA results for the $PA12_{AR4}$ spoiler is visible in Figure 13 and is also evident from the error in the comparison in Table 9. Specifically, this error ranges from 8.412% to 9.713% for vertical deflection, from -12.32% to -18.71% for horizontal deflection, and from -0.50% to -0.53% for the rotation angle. This is the only case where the error in the rotation angle between experimental and FEA results slightly decreases as the load increases.

Table 9. Comparison of slope endpoint for $PA12_{AR4}$ material

| $PL^2/EI$ | Vertical Deflection $PA12_{AR4}$ | | | Horizontal Deflection $PA12_{AR4}$ | | | Rotation $PA12_{AR4}$ | | |
|---|---|---|---|---|---|---|---|---|---|
| | $(u_y/L)$ FEA | $(u_y/L)$ Exp | Error | $(u_x/L)$ FEA | $(u_x/L)$ Exp | Error | $\phi_0$ FEA | $\phi_0$ Exp | Error |
| 0 | 0 | 0 | 0% | 0 | 0 | 0% | 0 | 0 | 0% |
| -16.459 | -0.04458 | -0.04083 | 8.412% | -0.00037 | -0.00032 | -12.32% | -0.04456 | -0.0443 | -0.53% |
| -32.918 | -0.08760 | -0.08003 | 8.634% | -0.00078 | -0.00067 | -13.05% | -0.08744 | -0.0869 | -0.53% |
| -49.378 | -0.12875 | -0.11684 | 9.243% | -0.00121 | -0.00103 | -15.34% | -0.12819 | -0.1275 | -0.53% |
| -65.837 | -0.16821 | -0.15238 | 9.413% | -0.00168 | -0.00142 | -15.93% | -0.16693 | -0.1660 | -0.53% |
| -82.296 | -0.20562 | -0.18581 | 9.635% | -0.00217 | -0.00181 | -17.02% | -0.20322 | -0.2021 | -0.53% |
| -98.756 | -0.24077 | -0.21747 | 9.678% | -0.00268 | -0.00221 | -17.91% | -0.23689 | -0.2356 | -0.51% |
| -115.21 | -0.27425 | -0.24769 | 9.683% | -0.00322 | -0.00263 | -18.20% | -0.26849 | -0.2671 | -0.51% |
| -131.67 | -0.30537 | -0.27571 | 9.713% | -0.00376 | -0.00306 | -18.71% | -0.29743 | -0.2959 | -0.50% |
| -148.13 | -0.3346 | -0.30879 | 7.714% | -0.00431 | -0.00375 | -12.91% | -0.32419 | -0.3224 | -0.53% |
| -164.59 | -0.36205 | -0.32688 | 9.713% | -0.00485 | -0.00394 | -18.71% | -0.34893 | -0.3472 | -0.50% |

In the case of the $PA12GB_{AR4}$ spoiler, the radius of curvature of the vertical deflection $u_y/L$ and the horizontal deflection $u_x/L$ are variable, and the deformation is not linear. The rotation angle ($\phi_0$), unlike $u_y/L$ and $u_x/L$, shows a linear section in the first part, ranging from 0 to -21.4887 $PL^2/EI$. It then becomes slightly curved in the second part, ranging from -21.4887 to -53.7217 $PL^2/EI$ (refer to Figure 14).

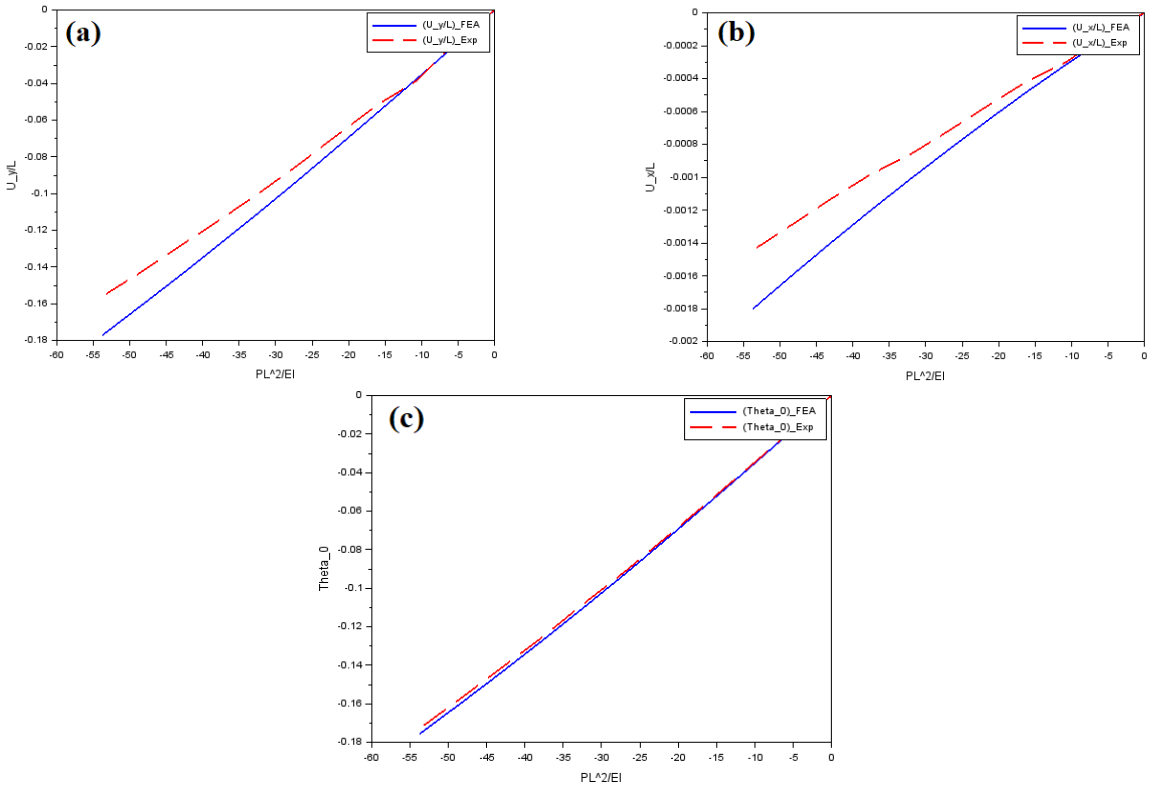


Figure 14. Comparison of $PA12GB_{AR4}$ (a) $u_y/L$ (b) $u_x/L$ and (c) $\phi_0$ of endpoint under various loads

Regarding the difference between experimental and FEA results for the $PA12GB_{AR4}$ spoiler, there is a divergence between them, with errors ranging from a minimum of 8.41% to a maximum of 11.94% for the vertical deflection $u_y/L$. In the case of horizontal deflection $u_x/L$, the error varies from a minimum of -12.32% to a maximum of -19.82%. Finally, in the case of rotation ($\phi_0$), the error varies from a minimum of -1.42% to a maximum of -1.60% (refer to Table 10).

Table 10. Comparison of slope endpoint for $PA12GB_{AR4}$ material

| $PL^2/EI$ | Vertical Defl. $PA12GB_{AR4}$ | | | Horizontal Defl. $PA12GB_{AR4}$ | | | Rotation $PA12GB_{AR4}$ | | |
|---|---|---|---|---|---|---|---|---|---|
| | $(u_y/L)$ FEA | $(u_y/L)$ Exp | Error | $(u_x/L)$ FEA | $(u_x/L)$ Exp | $(u_x/L)$ FEA | $\phi_0$ FEA | $\phi_0$ Exp | Error |
| 0 | 0 | 0 | 0% | 0 | 0 | 0% | 0 | 0 | 0% |
| -5.3722 | -0.0190 | -0.0174 | 8.412% | -0.00015 | -0.00013 | -12.32% | -0.01895 | -0.0187 | -1.42% |
| -10.744 | -0.0377 | -0.0387 | -2.59% | -0.00031 | -0.00029 | -4.843% | -0.03767 | -0.0371 | -1.46% |
| -16.116 | -0.0561 | -0.0518 | 7.812% | -0.00048 | -0.00042 | -13.20% | -0.05610 | -0.0553 | -1.43% |
| -21.488 | -0.0744 | -0.0678 | 8.941% | -0.00065 | -0.00056 | -13.53% | -0.07434 | -0.0733 | -1.40% |
| -26.860 | -0.0925 | -0.0842 | 8.970% | -0.00083 | -0.00072 | -13.74% | -0.09232 | -0.0910 | -1.41% |
| -32.233 | -0.1101 | -0.0996 | 9.570% | -0.00101 | -0.00086 | -14.84% | -0.10975 | -0.1077 | -1.84% |
| -37.605 | -0.1273 | -0.1142 | 10.36% | -0.00121 | -0.00098 | -18.24% | -0.12681 | -0.1250 | -1.42% |
| -42.977 | -0.1443 | -0.1283 | 11.05% | -0.00139 | -0.00113 | -19.06% | -0.14347 | -0.1411 | -1.62% |
| -48.349 | -0.1608 | -0.1425 | 11.43% | -0.00159 | -0.00128 | -19.32% | -0.15973 | -0.1571 | -1.61% |
| -53.721 | -0.1771 | -0.1559 | 11.94% | -0.00180 | -0.00144 | -19.82% | -0.17557 | -0.1727 | -1.60% |

### 3.5 General Discussions

#### 3.5.1 Linear vs. nonlinear deformation: A clarification

In the present study, classification into linear and nonlinear deformation regimes is based on experimentally measured stress-strain responses of the materials rather than on the curvature of the displacement-load graphs alone. The elastic limit for $PA12_{AR1}$ corresponds to a maximum tensile strain of about 0.5%, while in the case of $PA12GB_{AR1}$, the elastic regime extends up to 0.4% strain. Thus, loads that would produce strains below these limits were analyzed using both linear and nonlinear solvers, whereas a nonlinear formulation was used exclusively for loads exceeding these thresholds. A quantitative comparison of linear and nonlinear FEA solutions in the elastic regime indicates that the difference between the two approaches remains below 3%, which shows that the linear formulation is adequate to predict small deformations within that range. However, when the applied load exceeds the experimentally established elastic limits, the difference

between the solutions from the linear and nonlinear approaches increases rapidly, reaching 12–15% or more, depending on the metric, indicating the strong nonlinearity of the deformation behavior. Only the nonlinear formulation is able to provide an accurate prediction of the structural response in these cases. This methodology provides a framework for transitioning from linear to nonlinear deformation analysis based on material constitutive behavior. It is quantitatively validated, thereby enhancing the reliability of the numerical and experimental comparisons presented herein.

The above results are discussed based on the effect of material type and aspect ratio:

i) Effect of Material Type

Significant differences in mechanical response are observed in the cantilever loading of PA12 and PA12GB materials. A linear regime is observed for strains lower than 0.5% (low loads) in PA12, after which nonlinear deformation occurs. The increase in the magnitude of vertical deflection $u_y/L$, horizontal deflection $u_x/L$, and rotation is nonlinear beyond the elastic regime applied load, as captured in Figs. 6 and 7. The experimental measurements and FEA predictions yield maximum discrepancies of 6%-13% for vertical and horizontal displacements and rotations, as tabulated in Tables 3–5. The evident nonlinearity may be due to local material inhomogeneity, print tolerances, and minor compliance within the experimental boundary conditions.

In contrast, the glass-bead-reinforced variant, PA12GB, shows a predominantly linear response for the entire range of applied loads. This can be explained by the composite material's stiffer behavior, which delays the onset of nonlinear deformation. For PA12GB, deviations between the experimental and FEA results are relatively low, amounting to 7–12% for displacements and 7–8.5% for rotations (Figures 8–10, Tables 4 and 6). Overall, the PA12GB maintains higher stiffness, smaller nonlinear effects and more predictable behavior under cantilever loading, while PA12 demonstrates significant nonlinearities at higher loads.

ii) Effect of Aspect Ratio

The spoiler's response to deformation is significantly influenced by the aspect ratio. At AR1 (100 mm), PA12 is linear at low loads but nonlinear at increased loads, whereas PA12GB tends to remain linear within the same load magnitude. The vertical maximum deflection errors in AR1 vary between 6.11% and 9.31% for PA12 and 7.13% and 8.44% for PA12GB. Similarly, horizontal deflection and rotation show similar error trends. At AR2 (200 mm), the PA12 curve of $u_y/L$ depicts a nonlinear radius of curvature, while that of PA12GB maintains near linear trends. The horizontal deflection of both materials remains fairly linear. The increase in load increases the divergence between the experimental and FEA results. The vertical displacement errors range from 9.83% to 12.76%, while the rotation errors range from 9.81% to 12.72%, as listed in Table 6.

For AR3 (300 mm), nonlinear behavior is more accentuated in the case of PA12, for which vertical and rotational displacements show variable curvature. Maximum discrepancies between the experimental and finite element analysis results amount to 12.74% for $u_y/L$, -14.96% for $u_x/L$ and -12.7% for rotation (Tables 7–8). PA12GB features less steep slopes with smaller deviations from linearity. At AR4 (400 mm), PA12 exhibits all-round nonlinear deflection. The vertical deflection errors are in the range of 8.41% to 9.71%, horizontal from -12.32% to -18.71%, and rotation from -0.5% to -0.53% (Table 9). In the case of PA12GB, a combination of linear and slightly curved responses, the errors ranged from 8.41% to 11.94% for vertical deflection, -12.32% to -19.82% for horizontal deflection, and -1.42% to -1.6% for rotation (Table 10). These observations indicate that for higher aspect ratios, nonlinearity and increased displacement magnitude are strongly amplified, especially for PA12; PA12GB thus acts consistently towards nonlinear reduction and provides more uniform deformation.

iii) Experimental vs. FEA Comparison

Overall, the FEA predictions show good agreement with the experimental measurements for all aspect ratios and materials. These deviations tend to increase with increasing loads and larger aspect ratios, which can be attributed to several factors, including material property variations such as layer-wise inhomogeneity, local porosity and crystallinity differences; print tolerances like minor geometric deviation and surface finish irregularities; boundary compliance due to slight flexibility of the experimental fixture; and assumptions in FEA modelling, including element discretization and material isotropy. Despite these influences, maximum deviations always remain within acceptable limits ($\leq$ 19.82%), thus proving that the FEA model accurately captures both elastic and plastic responses of the spoiler.

iv) Comparison with Traditional Materials

Compared with the standard aluminium spoiler, the PA12 and PA12GB can achieve significant mass reduction for similar structural stiffness under low to moderate load conditions. In particular, PA12GB shows superior stiffness retention and reduced nonlinear deflection, pointing to the benefit of a reinforced polymer composite in lightweight automotive applications. These findings are expected to illustrate the potential of MJF-printed polymer-based spoilers in functional and high-performance automotive structures while offering design freedom and material efficiency.

## 4. CONCLUSIONS

This work presents an investigation into the deformation response of a high-camber automotive spoiler manufactured via Multi Jet Fusion 3D printing. The materials used for the study are Nylon PA12 and glass bead reinforced PA12 (PA12GB). The spoiler was tested in a cantilever-beam setup under different levels of concentrated loading, with deformations measured experimentally and verified with FEA. Mesh independence was ensured with a hexahedral SH3 mesh comprising 2,640 elements, with an average element quality of 0.9075 and aspect ratios ranging from 1.002 to 384.6. The results clearly show that PA12 undergoes significant nonlinear deformation, whereas PA12GB exhibits primarily linear behaviour, with vertical deflection as the dominant mode of deformation. Horizontal displacements and rotations remain considerably smaller. Comparisons between experimental and FEA results indicated very little discrepancy, proving the accuracy of the numerical predictions.

These results provide evidence that MJF-based 3D printing can enable rapid, cost-effective production of complex spoiler geometries with smooth surface finishes. It provides lightweight, structurally efficient solutions for automotive engineering applications. Such insight extends beyond the manufacturing of automotive components to the customized production of plastic parts in sectors such as lightweight robotics, biomedical devices, and flexible electronics. Future research directions include optimizing material reinforcement strategies, investigating other polymer composites, and integrating topological optimization with additive manufacturing to further improve structural performance and reduce weight, enabling broader applications in high-performance engineering sectors.

## ACKNOWLEDGEMENTS

This work was supported by Wuhan University of Technology, China. The authors gratefully acknowledge the resources and assistance provided by the institution.

## FUNDING

This study was not supported by any grants from funding bodies in the public, private, or not-for-profit sectors.

## CONFLICT OF INTEREST

The authors declare no conflicts of interest

## AUTHORS CONTRIBUTION

Luigi Buffone (Conceptualization, methodology, numerical test and validation, writing—original draft)

Georgios Manganos (Experimental test and Rewriting)

Kavitha Mol S. (Data curation, Writing- Review & Editing)

All authors have read and agreed to the published version of the manuscript

## REFERENCES

[1] I. Gibson, D. W. Rosen, and B. Stucker, *Additive Manufacturing Technologies: 3D Printing, Rapid Prototyping, and Direct Digital Manufacturing*, 3rd ed. New York, NY, USA: Springer, 2021.

[2] T. Bera, "A review on significant role of additive manufacturing in biomedical applications," *Advanced Materials & Sustainable Manufacturing*, vol. 1, no. 1, p. 10002, 2024.

[3] B. Blakey-Milner, P. Gradl, G. Snedden, M. Brooks, J. Pitot, E. Lopez, et al., "Metal additive manufacturing in aerospace: A review," *Materials & Design*, vol. 209, p. 110008, 2021.

[4] L. Zhou, J. Miller, J. Vezza, M. Mayster, M. Raffay, Q. Justice, et al., "Additive manufacturing: A comprehensive review," Sensors, vol. 24, no. 9, p. 2668, 2024.

[5] A. Bandyopadhyay and B. Heer, "Additive manufacturing of multi-material structures," Materials Science and Engineering R: Reports, vol. 129, pp. 1–16, 2018.

[6] A. Verma, A. Kapil, D. Klobčar, and A. Sharma, "A review on multiplicity in multi-material additive manufacturing: Process, capability, scale, and structure," Materials, vol. 16, no. 15, p. 5246, 2023.

[7] Setter, R. and Wudy, K., "Additive manufacturing and mechanical analysis of multi-material polymer parts combining thermosets and thermoplastics," *Advanced Composites and Hybrid Materials*, vol. 7, p. 122, 2024.

[8] A. C. Lopes, A. M. Sampaio, F. Fernandes, et al., "Design and industrial implementation of a multi-functional part produced by powder bed fusion," *Progress in Additive Manufacturing*, vol. 9, pp. 935–945, 2024.

[9] H. Eskandari Sabzi, S. Ahmadi, and M. Lajevardi, "Sustainable powder-based additive manufacturing: A review," *Sustainability*, vol. 15, no. 20, p. 15081, 2023.

[10] S. Rajendran, G. Palani, A. Kanakaraj, V. Shanmugam, A. Veerasimman, S. Gądek, et al., "Metal and polymer-based composites manufactured using additive manufacturing—A brief review," *Polymers*, vol. 15, no. 11, p. 2564, 2023.

[11] M. Balubaid and N. Alsaadi, "Achieving sustainability in manufacturing through additive manufacturing: An analysis of its enablers," *Sustainability*, vol. 15, no. 12, p. 9504, 2023.

[12] Y. Song, N. Hao, S. Ruan, C. He, and Q. Ma, "Free vibration properties of beetle elytron plate: Composite material, stacked structure and boundary conditions," *Mechanics of Materials*, vol. 185, p. 104754, 2023.

[13] Q. Ma, M. N. M. Merzuki, M. R. M. Rejab, M. S. M. Sani, and B. Zhang, "Numerical investigation on free vibration analysis of Kevlar/Glass/Epoxy resin hybrid composite laminates," *Malaysian Journal on Composites Science & Manufacturing*, vol. 9, no. 1, pp. 11–21, 2022.

[14] M. N. M. Merzuki, M. R. M. Rejab, M. S. M. Sani, B. Zhang, and M. Quanjin, "Experimental investigation of free vibration analysis on fibre metal composite laminates," *Journal of Mechanical Engineering and Sciences*, vol. 13, no. 4, pp. 5753–5763, 2019.

[15] J. Shu, J. Wang, Z. Li, and K.-Y. (Raymond) Tong, "Effects of slit edge notches on mechanical properties of 3D-printed PA12 nylon kirigami specimens," *Polymers*, vol. 15, no. 14, p. 3082, 2023.

[16] A. Avanzini, D. Battini, and S. Pandini, "Static and fatigue behavior in presence of notches for polyamide 12 (PA12) additively manufactured via multi jet fusion™ process," *International Journal of Fatigue*, vol. 161, p. 106912, 2022.

[17] J. Suder, Z. Bobovsky, J. Mlotek, M. Vocetka, Z. Zeman, and M. Safar, "Experimental analysis of temperature resistance of 3D printed PLA components," *MM Science Journal*, vol. 1, pp. 4322–4327, 2021.

[18] C. Cai, W. S. Tey, J. Chen, W. Zhu, X. Liu, T. Liu, L. Zhao, and K. Zhou, "Comparative study on 3D printing of polyamide 12 by selective laser sintering and multi jet fusion," *Journal of Materials Processing Technology*, vol. 288, p. 116882, 2021.

[19] V. Mazzanti, L. Malagutti, and F. Mollica, "FDM 3D printing of polymers containing natural fillers: A review of their mechanical properties," *Polymers*, vol. 11, p. 1094, 2019.

[20] T. Saksala, "A simple J2-plasticity-damage model for metals in the small strain regime," *Rakenteiden Mekaniikka*, vol. 45, no. 2, pp. 59-71, 2012.

[21] Q. Gu, J. P. Conte, Z. Yang and A. Elgamal, "Consistent tangent moduli for multi-yield-surface J2 plasticity model," *Computational Mechanics*, vol. 48, pp. 97-120, 2011.

[22] CompassIS, *CompassIS TDYN Theory Manual*, section "The J2 plasticity theory," 2021

[23] C. H. Wang and C. N. Duong, "Failure criteria," in *Bonded Joints and Repairs to Composite Airframe Structures*, Academic Press, 2016, pp. 21–45.

[24] X. Jiaotong, "Fracture assessment of polyamide 12 (PA12) specimens fabricated via Multi Jet Fusion in the presence of geometrical discontinuities," *Engineering Fracture Mechanics*, vol. 303, p. 110118, 2024.

[25] B. Hu, X. Chen, F. Deng, and X. Sun, "Evaluation of failure criteria for residual tensile strength of composite laminates with circular holes," *Vibroengineering Procedia*, vol. 33, pp. 34–41, 2023.

[26] K. Ráž, Z. Chval, and S. Thomann, "Minimizing deformations during HP MJF 3D printing," *Materials*, vol. 16, p. 7389, 2023.

[27] T. Heitkamp, S. Girnth, S. Kuschmitz, N. Waldt, G. Klawitter, and T. Vietor, "Experimental and numerical investigation of the mechanical properties of 3D-printed hybrid and non-hybrid composites," *Polymers*, vol. 15, p. 1164, 2023.

[28] D. Singhal and V. Narayanamurthy, "Large and small deflection analysis of a cantilever beam," *Journal of the Institution of Engineers (India): Series A*, vol. 100, no. 1, pp. 83–96, 2019.

[29] A. E. H. Love, *The Mathematical Theory of Elasticity*. New York, NY, USA: Dover, 1944

[30] R. Frisch-Fay, *Flexible Bars*. London, U.K.: Butterworths, 1962.

[31] J. M. Gere and S. P. Timoshenko, *Mechanics of Materials*. New York, NY, USA: McGraw-Hill, 1972.

[32] C. T. Noh, K. Smith, C. L. Shamo, J. Porter, K. Steele, N. D. Ludlow, et al., "Measurement of force and position using a cantilever beam and multiple strain gauges: Sensing principles and design considerations," *Sensors*, vol. 25, no. 21, p. 6561, 2025.

[33] S. Kumar, T. Kolekar, S. Patil, A. Bongale, K. Kotecha, A. Zaguia, and C. Prakash, "A low-cost multi-sensor data acquisition system for fault detection in fused deposition modelling," *Sensors*, vol. 22, no. 2, p. 517, 2022.

[34] A. Earij, G. Alfano, K. Cashell, and X. Zhou, "Nonlinear three-dimensional finite-element modelling of reinforced-concrete beams: Computational challenges and experimental validation," *Engineering Failure Analysis*, vol. 82, pp. 92–115, 2017.

[35] A. V. Kumar, S. Padmanabhan, and R. Burla, "Implicit boundary method for finite element analysis using non-conforming mesh or grid," *International Journal for Numerical Methods in Engineering*, vol. 74, no. 9, pp. 1421–1447, 2007.